Neurobiology of Aging 36 (2015) S132–S140

Contents lists available at ScienceDirect

Neurobiology of Aging

journal homepage: www.elsevier.com/locate/neuaging

Network and connectivity

Diffusion weighted imaging-based maximum density path analysis and classification of Alzheimer's disease

Talia M. Nir [a,1], Julio E. Villalon-Reina [a,1], Gautam Prasad [a], Neda Jahanshad [a], Shantanu H. Joshi [b], Arthur W. Toga [a], Matt A. Bernstein [c], Clifford R. Jack Jr [c], Michael W. Weiner [d], Paul M. Thompson [a,e,f,g,h,i,j,*], for the Alzheimer's Disease Neuroimaging Initiative (ADNI)[2]

[a] Imaging Genetics Center, Institute for Neuroimaging & Informatics, University of Southern California, Los Angeles, CA, USA
[b] Department of Neurology, UCLA School of Medicine, Los Angeles, CA, USA
[c] Department of Radiology, Mayo Clinic and Foundation, Rochester, MN, USA
[d] Department of Radiology and Biomedical Imaging, UCSF School of Medicine, San Francisco, CA, USA
[e] Department of Neurology, University of Southern California, Los Angeles, CA, USA
[f] Department of Psychiatry, University of Southern California, Los Angeles, CA, USA
[g] Department of Radiology, University of Southern California, Los Angeles, CA, USA
[h] Department of Engineering, University of Southern California, Los Angeles, CA, USA
[i] Department of Pediatrics, University of Southern California, Los Angeles, CA, USA
[j] Department of Ophthalmology, University of Southern California, Los Angeles, CA, USA

ARTICLE INFO

Article history:
Received 2 May 2013
Received in revised form 13 May 2014
Accepted 13 May 2014
Available online 27 August 2014

Keywords:
ADNI
Tractography
DTI
Fiber tract modeling
White matter
Connectivity
SVM
Classification

ABSTRACT

Characterizing brain changes in Alzheimer's disease (AD) is important for patient prognosis and for assessing brain deterioration in clinical trials. In this diffusion weighted imaging study, we used a new fiber-tract modeling method to investigate white matter integrity in 50 elderly controls (CTL), 113 people with mild cognitive impairment, and 37 AD patients. After clustering tractography using a region-of-interest atlas, we used a shortest path graph search through each bundle's fiber density map to derive maximum density paths (MDPs), which we registered across subjects. We calculated the fractional anisotropy (FA) and mean diffusivity (MD) along all MDPs and found significant MD and FA differences between AD patients and CTL subjects, as well as MD differences between CTL and late mild cognitive impairment subjects. MD and FA were also associated with widely used clinical scores. As an MDP is a compact low-dimensional representation of white matter organization, we tested the utility of diffusion tensor imaging measures along these MDPs as features for support vector machine based classification of AD.

1. Introduction

Alzheimer's disease (AD) is the most common type of dementia, affecting around 1 in 8 people aged 65 years or older in the United States alone (Alzheimer's Association, 2011). AD is characterized by cortical and hippocampal neuronal loss and widespread gray matter atrophy, but there is also a progressive disconnection of cortical and subcortical regions because of white matter (WM) injury (Delbeuck et al., 2003). Changes in WM neuropathology include partial loss of axons and myelin sheaths (Brun and Englund, 1986; Sjobeck et al., 2005). AD patients show significant WM atrophy (Hua X et al., 2008, 2010; Migliaccio et al., 2012), as well as a gradual decrease in the integrity of WM commissures such as the corpus callosum, and key pathways such as the cingulum and superior longitudinal fasciculus (Liu et al., 2011; Medina et al., 2006; Rose et al., 2000; Stebbins and Murphy, 2009).

In addition to the more widely used measures from anatomic magnetic resonance imaging (MRI), fluorodeoxyglucose- and amyloid-positron emission tomography, and cerebrospinal spinal

* Corresponding author at: Imaging Genetics Center, Institute for Neuroimaging and Informatics, Keck/USC School of Medicine, University of Southern California, Los Angeles, CA, USA. Tel.: +1 323 442 7246; fax: +1 323 442 7247.
E-mail address: pthomp@usc.edu (P.M. Thompson).
[1] These authors contributed equally to this work.
[2] Many investigators within the ADNI contributed to the design and implementation of ADNI and/or provided data, but most of them did not participate in analysis or writing of this report. A complete list of ADNI investigators may be found at: http://adni.loni.usc.edu/wp-content/uploads/how_to_apply/ADNI_Acknowledgement_List.pdf.

0197-4580/$ – see front matter © 2015 Elsevier Inc. All rights reserved.
http://dx.doi.org/10.1016/j.neurobiolaging.2014.05.037

based measures of pathology, the second phase of the Alzheimer's Disease Neuroimaging Initiative (ADNI-2) includes additional neuroimaging measures including diffusion weighted imaging (DWI) in a subset of the imaged population. By tracking the highly anisotropic diffusion of water along axons, DWI can be used to evaluate the integrity and trajectory of the major WM fiber bundles in the brain. DWI is sensitive to microscopic WM injury in these bundles and may identify signs of impairment in anatomic connectivity that are not detectable with standard anatomic MRI.

Current methods for DWI analysis, including voxelwise analysis, region-of-interest (ROI) analysis, tract-based spatial statistics (TBSS; Smith et al., 2006), and tractography, are limited, to some extent, by how well each method can identify comparable brain regions and tracts across subjects. Here, we used a new tract clustering and registration method that combines the strengths of voxelwise and tractography-based methods, yielding a compact representation of fiber bundles. Like other cross-subject fiber-based methods (Colby et al., 2012), it also computes cross-subject correspondences for group comparisons. To compare tracts across subjects, tracts are often clustered into anatomic groups. Numerous clustering methods have been applied to tractography, including generalized Procrustes analysis (Corouge et al., 2006), spectral clustering (O'Donnell et al., 2006), Dirichlet distributions (Maddah et al., 2008), and Gaussian process frameworks (Wassermann et al., 2010). This method uses maximum density paths (MDPs) based on whole-brain tractography (Prasad et al., 2011a, 2011b, 2013a). Unlike some prior clustering methods, the large collection of tractography-generated 3D curves is first organized into bundles using prior anatomic landmarks to identify WM tracts based on a probabilistic WM atlas (Hua KJ et al., 2008). These bundles are then reduced to a single MDP by computing a path through the points of the highest streamline density. The paths are then matched across subjects using geodesic curve registration (Joshi et al., 2007a, 2007b) for statistical comparison. This method avoids some of the pitfalls of methods that rely on traditional whole-brain nonlinear registration, such as TBSS and voxel-based analysis, which arguably may introduce bias (Schwarz et al., 2014; Tustison et al., 2014). Additionally, many tract clustering methods ultimately collapse the diffusion tensor imaging (DTI) metrics along each tract into a single summary mean value for statistical analysis. By using along-tract pointwise statistics, we can detect localized differences within a single tract. The use of pointwise statistics on 3D curves has been quite popular in the engineering literature, but articles using other methods (such as TBSS) far outnumber them in the neuroimaging literature. The use of pointwise statistics on tract curves is also mathematically related to work over the last 2 decades on the averaging and comparison of sulcal curves on the cortex, represented as 3D space curves or as parametric surfaces (Thompson et al., 1996a, 1996b; Zhou et al., 1999; Fillard et al., 2006; Shi et al., 2007).

In our present study, differences in WM microstructure were determined by comparing fractional anisotropy (FA) and mean diffusivity (MD) point-wise along each MDP between normal control (CTL) subjects and either mild cognitive impairment (MCI) or AD patients. We also examined associations between FA and MD along these paths with a widely used cognitive rating, the Mini-Mental State Examination (MMSE; Folstein et al., 1975). As an MDP is a low-dimensional representation of the white matter organization, we further assessed whether the DTI measures interpolated along the MDP were useful features for a support vector machine (SVM; Cortes and Vapnik, 1995) based classification of AD.

2. Methods

2.1. Image acquisition and subject information

Data collection for the ADNI-2 project is still in progress. Here, we performed an initial analysis of data from 200 participants, of whom 50 were CTL, 113 had MCI, and 37 were AD patients (Table 1). We note that in ADNI-2, MCI participants include the enrollment of a new early MCI (e-MCI) cohort, with milder episodic memory impairment than the MCI group of ADNI-1, now called late MCI (l-MCI) in ADNI-2. Each subject underwent a cognitive evaluation using the MMSE (scores of less than 24 of 30 indicate impairment; Folstein et al., 1975). Detailed inclusion and exclusion criteria are found in the ADNI2 protocol (http://adni-info.org/Scientists/Pdfs/ADNI2_Protocol_FINAL_20100917.pdf).

All subjects underwent whole-brain MRI scanning on 3-Tesla GE Medical Systems scanners at 14 acquisition sites across North America. T1-weighted inversion recovery fast spoiled gradient echo (spoiled gradient echo) anatomic scans were collected (256 × 256 matrix; voxel size = 1.2 × 1.0 × 1.0 mm^3; inversion time = 400 ms; repetition time = 6.98 ms; echo time = 2.85 ms; flip angle = 11°), as well as diffusion-weighted images (DWI; 35 cm field of view, 128 × 128 acquired matrix, reconstructed to a 256 × 256 matrix; voxel size: 2.7 × 2.7 × 2.7 mm^3; scan time = 9 minutes; more imaging details may be found at http://adni.loni.usc.edu/wp-content/uploads/2010/05/ADNI2_GE_3T_22.0_T2.pdf). Forty-six separate images were acquired for each DWI scan: 5 T2-weighted images with no dedicated diffusion sensitization (b_0 images) and 41 diffusion-weighted images (b = 1000 s/mm^2). This ADNI protocol was chosen after conducting a detailed comparison of several different DTI protocols, to optimize the signal-to-noise ratio in a fixed scan time (Jahanshad et al., 2010; Zhan et al., 2013). All T1-weighted MR and DWI images were visually checked for quality assurance to exclude scans with excessive motion and/or artifacts; all scans were included.

2.2. Image preprocessing

For each subject, all baseline raw DWI volumes were aligned with the FSL eddy-correct tool (http://www.fmrib.ox.ac.uk/fsl) to correct for head motion and eddy-current distortions. All extracerebral tissue was subsequently removed from diffusion-weighted images using the Brain Extraction Tool from FSL (Smith, 2002). Non-brain tissue was also removed from T1-weighted anatomic scans using both ROBEX, a robust automated brain extraction program trained on manually "skull-stripped" MRI data

Table 1
Demographics and clinical scores for the participants

	CTL (n = 50)	MCI (n = 113)	e-MCI (n = 74)	l-MCI (n = 39)	AD (n = 37)	*p*-value for group difference		
						CTL versus MCI	e-MCI versus l-MCI	CTL versus AD
Age	72.1 ± 5.9	72.6 ± 7.4	72.8 ± 8.1	72.4 ± 5.8	75.7 ± 9.3	0.66	0.75	0.05
Sex (M/F)	22/28	70/43	46/28	24/15	21/16	**0.04**	0.95	0.24
MMSE	28.8 ± 1.5	27.8 ± 1.7	28.1 ± 1.5	27.2 ± 1.9	23.0 ± 2.0	8.48×10^{-5}	**0.01**	2.44×10^{-22}

Bold indicates significance (i.e. $p < 0.05$).
Key: AD, Alzheimer's disease; CTL, controls; e-MCI, early mild cognitive impairment; F, female; l-MCI, late mild cognitive impairment; M, male; MMSE, Mini-Mental State Examination.

(Iglesias et al., 2011) and FreeSurfer (Fischl et al., 2004). Skull-stripped volumes were visually inspected, and the best extraction selected, including both cerebellum and brain stem. Images were then further manually delineated by a trained anatomist to further remove any scalp, meninges, or neck not automatically removed. Anatomic scans subsequently underwent intensity inhomogeneity normalization using the MNI nu_correct tool (www.bic.mni.mcgill.ca/software/). To align data from different subjects into the same 3D coordinate space, each anatomic image was linearly aligned to a standard brain template (the downsampled Colin27: 110 × 110 × 110, with 2 mm isotropic voxels; Holmes et al., 1998) using FSL flirt (Jenkinson et al., 2002) with 6 degrees of freedom to allow only translations and rotations in 3D.

To correct for echo-planar imaging (EPI) induced susceptibility artifacts, which can cause distortions at tissue-fluid interfaces, skull-stripped *b0* (non–diffusion weighted) images were linearly aligned and then elastically registered to their respective T1-weighted structural scans (in the Colin27 110 × 110 × 110 space) using an inverse-consistent registration algorithm with a mutual information cost function (Leow et al., 2007). The resulting linear 3D transformation matrices and 3D deformation fields were then applied to the remaining 41 DWI volumes, so that the DWIs and respective T1 images were in the same space.

A single diffusion tensor was fitted at each voxel in the brain from the eddy- and EPI-corrected DWI scans using FSL, and scalar anisotropy maps were obtained (Basser et al., 1994) from the resulting diffusion tensor eigenvalues (λ_1, λ_2, and λ_3). FA, a measure of the degree of diffusion anisotropy, was defined in the standard way as:

$$FA = \sqrt{\frac{3}{2}} \frac{\sqrt{(\lambda_1 - <\lambda>)^2 + (\lambda_2 - <\lambda>)^2 + (\lambda_3 - <\lambda>)^2}}{\sqrt{\lambda_1^2 + \lambda_2^2 + \lambda_3^2}}$$

$$\in [0, 1]$$

$$<\lambda> = \frac{\lambda_1 + \lambda_2 + \lambda_3}{3}$$

where $<\lambda>$ is equal to the MD or average rate of diffusion in all directions. The resulting images were smoothed with a Gaussian kernel (5 mm full width at half maximum) to improve the signal-to-noise ratio and ensure a Gaussian distribution of the maps. Clearly, other smoothing filters could be used, or, at the expense of added complexity, the full diffusion image data could be filtered to preserve maximal information (Cetingul et al., 2014; Kim et al., 2009; Tong et al., 2012).

2.3. Fiber tractography

At each voxel, constant solid angle orientation distribution functions (CSA-ODFs) were computed using the normalized and dimensionless ODF estimator, derived for Q-ball imaging as in Aganj et al. (2010). Tractography was performed on the linearly aligned sets of DWI volumes (in the Colin27 110 × 110 × 110 space) by probabilistically seeding voxels with a prior probability based on the FA value. Curves through a seed point receive a score estimating the probability that they follow an axonal pathway, computed from the CSA-ODFs. We used a voting process provided by the Hough transform to determine the best fitting curves through each point, based on using a constant solid angle orientation density function to model the local diffusion propagator (Aganj et al., 2011); the resulting tractography is illustrated in Fig. 1A. Elastic deformations obtained from EPI distortion correction, mapping the average b_0 image to the T1-weighted image, were then applied to the resulting tracts' 3D coordinates. Each subject's data set contained about 10,000 non-duplicated fibers (3D curves). In prior work, we have determined that this is a sufficient number of fibers to determine most of the common network topology measures accurately (Prasad et al., 2013b). We removed any erroneous fibers traced on the edge of the brain because of high intensity noise. To limit small noisy tracts, we filtered out fibers with less than 10 points.

The angular resolution of the ADNI data is deliberately limited to avoid long scan times that increase patient attrition, but the use of an ODF model makes best use of the available angular resolution. The ODF-CSA model ensures a high-quality tractography, which is the crux of the MDP methodology, but other validated methods could be used. Methods that can resolve more than 1 intravoxel dominant diffusion direction, such as q-ball imaging, spherical deconvolution based methods, and diffusion spectrum imaging (DSI), tend to perform better than DTI when used to reconstruct tracts, and they may better reflect the underlying anatomy when more than 1 tract is present (Daducci et al., 2014; Tuch, 2004). Once the 3D geometry of the tracts has been extracted, any number of features can be interpolated onto the tract-derived MDPs.

2.4. Probabilistic white matter ROI atlas registration and fiber clustering

Fibers were clustered into 18 ROIs using the Johns Hopkins University (JHU) probabilistic WM tract atlas (Hua KJ et al., 2008). A trained anatomist created up to 3 pairs of seed points (each pair consists of 1 start and 1 end seed; Fig. 1C) for each ROI tract based on the anatomy and the highest probability at the extremities of

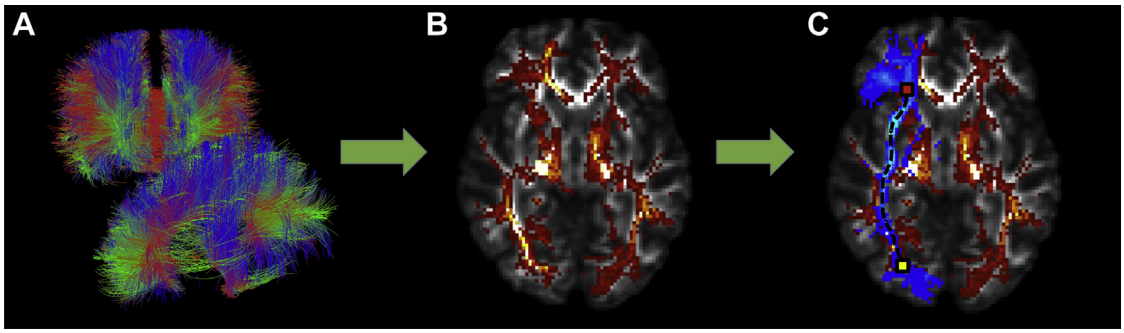

Fig. 1. (A) Whole-brain tractography fibers derived using the Hough transform method, based on DWI data from one individual in the study. (B) Whole-brain tractography was converted into a fiber density map (red/yellow), where each voxel in the volume represents the total number of streamlines that pass through it. (C) Probabilistic ROI (blue; right inferior fronto-occipital fasciculus) overlaid on the fiber density map (red/yellow). The MDP algorithm finds the shortest path through the fiber density map within the boundaries of the ROI from a start seed (yellow) to an end seed (red). Abbreviations: DWI, diffusion-weighted images; MDP, maximum density path; ROI, region of interest. (For interpretation of the references to color in this Figure, the reader is referred to the web version of this article.)

Table 2
Index of ROIs from the probabilistic tract atlas (Hua KJ et al., 2008) used for analysis, followed by their abbreviations, and the number of sets of seeds

Corpus callosum through		
Cingulum	CC-Cing	2
Cuneus	CC-Cu	1
Lingual gyrus	CC-LG	1
Middle frontal gyrus	CC-MFG	1
Middle occipital gyrus	CC-MOG	1
Postcentral gyrus	CC-PoCG	1
Precentral gyrus	CC-PrCG	1
Precuneus	CC-PrCu	1
Rectal gyrus	CC-RG	1
Superior frontal gyrus	CC-SFG	3
Superior occipital gyrus	CC-SOG	1
Superior parietal gyrus	CC-SPG	1
Bilateral		
Cingulum at the cingulate gyrus	CGC	1
Cingulum at the hippocampus	CGH	1
Inferior fronto-occipital fasciculus	IFO	1
Inferior longitudinal fasciculus	ILF	1
Superior longitudinal fasciculus	SLF	1
Uncinate fasciculus	UNC	1

Key: ROIs, regions of interest.

each tract (Table 2). We linearly aligned (Jenkinson et al., 2002) and then elastically registered (Leow et al., 2007) the FA image from the JHU DTI atlas to each subject's FA map. We then applied that deformation to both the WM atlas labels and the respective seed points, using nearest neighbor interpolation to avoid intermixing of labels. This placed the atlas ROIs and seeds in the same coordinate space as each subject's tractography (all in the Colin27 110 × 110 × 110 space). The ROIs were then smoothed with a Gaussian kernel (2 mm full width at half maximum) to ensure the registered ROIs were contiguous. We were then able to select all fibers that intersected each ROI, forming an ROI fiber bundle (Fig. 1C).

2.5. MDP computation

As described in Prasad et al. (2011a), (2011b), (2013a), each ROI fiber bundle for each subject was reduced to a compact low-dimensional representation based on the MDP. Using each subject's tractography, we generated a respective scalar fiber density map, where each voxel in the volume represents the total number of fibers that pass through it (Fig. 1B). From this density map, we created a graph, where each density map voxel greater than 0 was represented as a node that is connected to its surrounding 26 neighbors by weighted undirected edges. To make the cost of traveling from one node to another inversely proportional to their density, each edge was weighted by taking the negative of the sum of the density values from the 2 voxels it connected, as follows:

$$-(d_i + d_j) + em$$

here, *di* and *dj* denote node *i* and *j*'s corresponding voxel density. *em* is the maximum absolute value of the edge costs, added to ensure that the edges are positive.

Using each set of registered ROI seeds, delineating a start and end location, we did a graph search using an algorithm by Dijkstra (1959) to find the shortest path (i.e., the maximum density path). However, in cases where the seeds did not correspond to a node (i.e., at a nonzero density voxel), we found the closest voxel to the ROI seeds as determined by the Euclidean distance. In situations where there was a "hole" in the density map within an ROI because of the partial volume effect or the assignment of tracts into individual voxels, the algorithm could not create a connection between 2 nodes. We therefore added both nodes and edges, weighted with the smallest value possible, to the graph so all voxels within our ROI were fully connected (Jahanshad et al., 2012). This allowed gaps to be filled in without biasing the resulting shortest path.

2.6. MDP geodesic curve registration

As subjects were registered to the Colin27 template with a 6 parameter affine transform, the 3-dimensional MDP curves of each subject are confounded by nuisance variables such as translation and orientation. However, to assess cross subject correspondences for group comparisons of the compact MDP representations, the MDPs must be registered to a common space, while maintaining, as much as possible, the particular characteristics of each subject's anatomy. As in Joshi et al. (2007a), (2007b) , we analyzed their geometry intrinsically, and represented each MDP curve $\beta(s)$: [0,1] $\rightarrow \Re^3$ by its invariant shape given by the square-root velocity function as.

$$q(s) = \frac{\dot{\beta}(s)}{\sqrt{\left\|\dot{\beta}(s)\right\|}} \in \Re^3$$

The q function is a parameterized function and is invariant to translation and rotation. We also make it scale invariant by dividing it by its magnitude. The set of MDPs are represented by their q function representations in an invariant shape space, given by an infinite-dimensional Hilbert sphere of functions. This shape space is equipped with an invariant Riemannian metric that allows us to compute distances between shapes via the shortest paths or geodesics between them. The geodesic framework also allows us to compute invariant, intrinsic statistics (Joshi et al., 2007a, 2007b; Prasad et al., 2011a) on the space of MDP paths. Moreover, we align the MDP representations elastically by a diffeomorphic matching of their shapes. The elastic MDP shape registration uses an efficient path-straightening method (Joshi et al., 2007b) that computes geodesics between 2 tract representations in a few milliseconds. For our data, we calculated mean MDPs across all 200 subjects and elastically registered all the respective MDPs to the mean. We could then calculate group statistics for cross subject comparisons of any number of scalar attributes along these paths. We chose to interpolate corresponding features from more traditional scalar FA and MD maps at each point in the registered paths, as these indices are perhaps most likely to be used in standardized multisite DTI analyses. However, in future work we intend to also interpolate ODF based metrics, such as generalized FA (GFA), quantitative FA (QFA), and tensor distribution function (TDF) based FA (Leow et al. 2009; Tuch et al. 2004; Yeh et al. 2010; Zhan et al. 2009).

For each subject, the respective FA and MD values were interpolated at each point along the MDP via the linear interpolation function implemented in Matlab (http://www.mathworks.com/help/matlab/ref/interp3.html). We opted not to use cubic or spline interpolation that can sometimes result in negative values, as this would not make sense for FA values that range from 0 to 1. Some other works treat diffusion functions or diffusion tensors as elements of Riemannian manifolds, so many more elaborate interpolation choices are possible (Cetingul et al., 2014; Kim et al., 2009; Tong et al., 2012).

2.7. Statistical analyses

We performed pointwise linear regressions along each MDP, adjusting for sex and age, to test for differences in FA and MD between CTL and MCI subjects (e-MCI and l-MCI separately and as a whole) and between CTL and AD patients. We additionally tested for associations between FA and MD along each MDP and MMSE

scores in the entire population (n = 200), again adjusting for sex and age. Computing multiple association tests along each (floating point) voxel of an MDP path can introduce a high false positive error rate. To control the expected rate of these errors across all points within all paths, we used the standard method for false discovery rate (FDR) correction with the conventional q-value of 0.05 (Benjamini and Hochberg, 1995).

2.8. Post hoc classification

We used SVMs (Cortes and Vapnik, 1995), a type of supervised machine learning algorithm, to classify the DTI measures along the points of the mean MDPs to differentiate between diagnosis groups. SVMs classify 2-class data by learning to find the best hyperplane to separate the 2 classes by maximizing the distance between the hyperplane and the closest data point. Each subject is represented as a d-dimensional vector, x_i, and its category as $y_i = \pm 1$ to find the hyperplane.

$$y_i(< w; x_i > + b) \geq 1$$

such that w and b minimize $||w||$ for all x_i and y_i. In addition, we used nonlinear SVM classification by applying a nonlinear transformation using Gaussian radial basis functions.

Using accuracy, sensitivity, and specificity, we tested the utility of different subsets of features to distinguish between the 2 pairs of diagnostic groups where significant group differences were detected: CTL and AD, and CTL and l-MCI. In each fold of a 10 × 10-fold cross-validation, we randomly selected an equal number of subjects from each class to avoid the "unequal training class size bias" (Chew et al., 2001). We determined the subsets of features for each class pair based on the DTI measures (FA and/or MD) that showed significant differences between the groups. To distinguish between CTL and AD groups, we tested the FA values and MD values along all the mean MDP points (1080 points; Table 3). We further tested only the subset of significant FA points (FAFDR CvA = 214 points) and the subset of significant MD points (MDFDR CvA = 641 points). To distinguish between CTL and l-MCI we tested all the MD values along all the MDP points (1080 points), as well the subset of significant MD points (MDFDR CvL = 12 points).

3. Results

3.1. MDP analyses

AD patients showed significantly lower FA (Fig. 2A; critical $p < 0.01$) and higher MD (Fig. 2B; critical $p < 0.03$) compared with cognitively healthy elderly CTL subjects, throughout the commissural and long association fibers (Table 3). We found significantly higher MD in l-MCI subjects compared with CTL subjects (Fig. 2C; critical $p < 0.001$) in posterior and temporal lobe tracts. We did not detect differences between e-MCI (or the full MCI group) relative to the group of CTL subjects. These results are in the expected direction, as deteriorations in fiber integrity are generally accompanied by higher values for diffusivity measures.

We further found a significant positive association between FA and MMSE (Fig. 2D; critical $p < 0.003$) and negative association between MMSE and MD (Fig. 2E; critical $p < 0.029$). That is, lower FA and higher diffusivity, which typically indicate greater WM deficits, were associated with lower MMSE scores, which are indicative of greater cognitive impairment.

Table 3
Table of ROIs that exhibit FDR-significant (Benjamini and Hochberg, 1995) differences between CTL and either AD or l-MCI subjects and associations with MMSE cognitive scores. Here, we show the total length of each tract's mean MDP, as well the number of points that are FDR significant followed by the percentage of mean MDP tract points that show significant group differences

ROI	Total MDP Length	AD versus CTL		CTL versus l-MCI		MMSE	
		FA	MD	FA	MD	FA	MD
		$p < 0.010$ (%)	$p < 0.030$ (%)	—	$p < 0.001$ (%)	$p < 0.003$ (%)	$p < 0.029$ (%)
CGC L	59	23 (39.0)	22 (37.3)	—	—	2 (3.4)	16 (27.1)
CGC R	64	11 (17.2)	11 (17.2)	—	—	5 (7.8)	10 (15.6)
CGH L	25	—	22 (88.0)	—	—	—	21 (84.0)
CGH R	18	5 (27.8)	18 (100)	—	2 (11.1)	—	18 (100)
IFO L	67	12 (17.9)	45 (67.2)	—	—	5 (7.5)	51 (76.1)
IFO R	60	2 (3.3)	45 (75.0)	—	—	10 (16.7)	44 (73.3)
ILF L	42	5 (11.9)	35 (83.3)	—	3 (7.1)	—	42 (100)
ILF R	42	—	42 (100)	—	—	—	38 (90.5)
SLF L	35	—	18 (51.4)	—	—	—	20 (57.1)
SLF R	33	—	24 (72.7)	—	—	—	29 (87.9)
UNC L	23	6 (26.1)	23 (100)	—	2 (8.7)	3 (13.0)	22 (95.7)
UNC R	19	—	15 (78.9)	—	—	—	18 (94.7)
CC-Cing	71	10 (14.1)	21 (29.6)	—	—	—	23 (32.4)
CC-Cu	31	5 (16.1)	13 (41.9)	—	—	—	5 (16.1)
CC-LG	37	2 (5.4)	24 (64.9)	—	3 (8.1)	—	15 (40.5)
CC-MFG	25	5 (20.0)	17 (68.0)		—	3 (12.0)	18 (72.0)
CC-MOG	58	11 (19.0)	20 (34.5)	—	—	2 (3.4)	29 (50.0)
CC-PoCG	42	21 (50.0)	30 (71.4)	—	—	—	18 (42.9)
CC-PrCG	42	8 (19.0)	22 (52.4)	—	—	—	15 (35.7)
CC-PrCu	41	25 (61.0)	30 (73.2)	—	2 (4.9)	16 (39.0)	34 (82.9)
CC-RG	29	1 (3.4)	27 (93.1)	—	—	—	29 (100)
CC-SFG	120	25 (20.8)	57 (47.5)	—	—	4 (3.3)	57 (47.5)
CC-SOG	58	14 (24.1)	32 (55.2)	—	—	—	26 (44.8)
CC-SPG	39	23 (59.0)	28 (71.8)	—	—	15 (38.5)	27 (69.2)

Key: AD, Alzheimer's disease; CC, corpus callosum; CGC, cingulum at the cingulate gyrus, CGH, cingulum at the hippocampus; Cing, cingulum; CTL, controls; Cu, cuneus; FA, fractional anisotropy; FDR, false discovery rate; IFO, inferior fronto-occipital fasciculus; ILF, inferior longitudinal fasciculus; L, left; LG, lingual gyrus; l-MCI, late mild cognitive impairment; MD, mean diffusivity; MDP, maximum density path; MFG, middle frontal gyrus; MMSE, Mini-Mental State Examination; MOG, middle occipital gyrus; PoCG, postcentral gyrus; PrCG, precentral gyrus; R, right; RG, rectal gyrus; ROI, region of interest; SFG, superior frontal gyrus; SLF, superior longitudinal fasciculus; SOG, superior occipital gyrus; SPG, superior parietal gyrus.

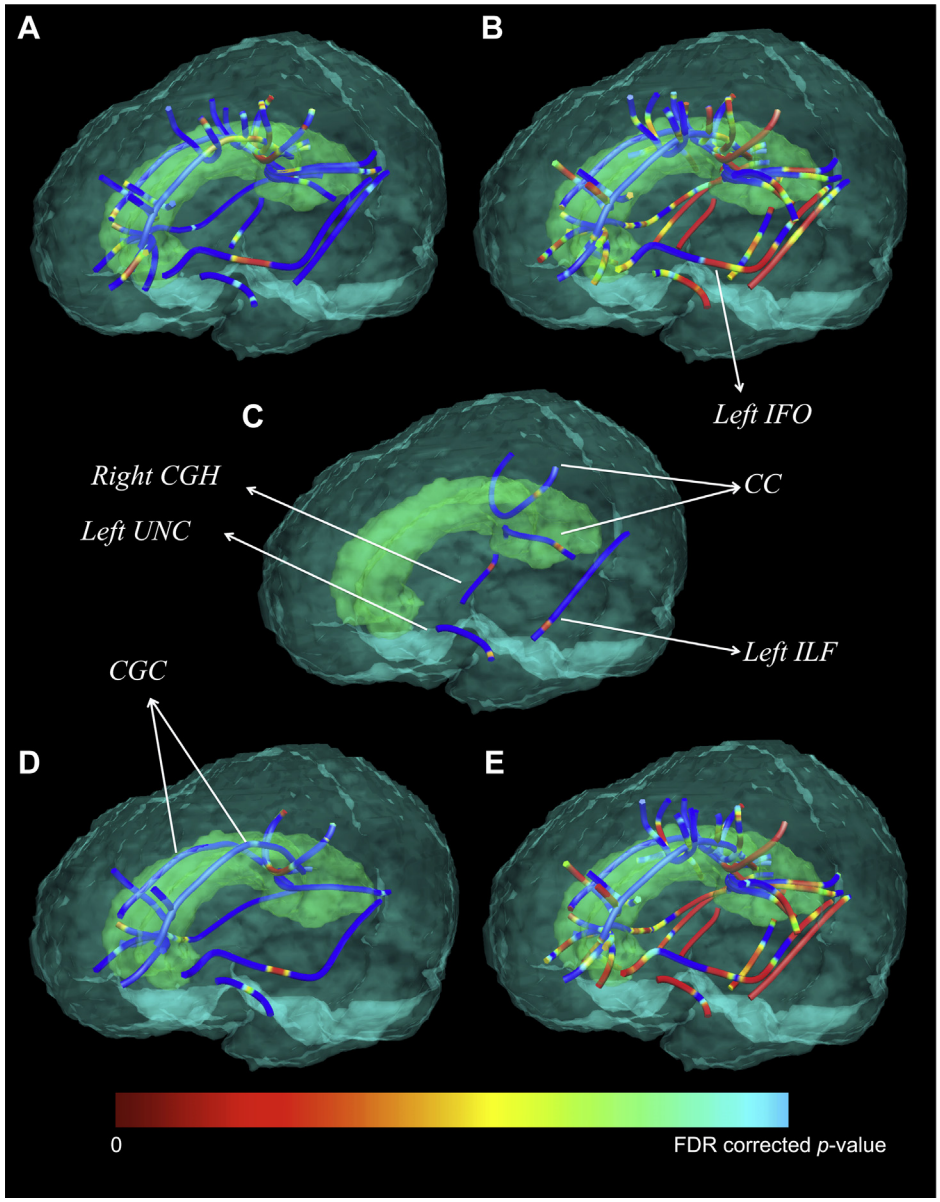

Fig. 2. Statistical maps show MDPs where (A) FA is significantly lower (critical $p < 0.01$) and (B) MD is significantly higher (critical $p < 0.03$) in AD patients compared with CTL subjects. (C) The MDPs are depict significantly higher MD in l-MCI compared with CTL subjects (critical $p < 0.001$). (D) MMSE was significantly positively associated with FA (critical $p < 0.003$) and (E) significantly negatively associated with MD (critical $p < 0.029$) in the entire population (n = 200). In this figure, the color bar upper value (i.e., blue FDR corrected *p*-value) corresponds to a different FDR critical *p*-value for each analysis (A–D). Abbreviations: AD, Alzheimer's disease; CC, corpus callosum; CGC, cingulum at the cingulate gyrus, CGH, cingulum at the hippocampus; CTL, controls; FA, fractional anisotropy; FDR, false discovery rate; IFO, inferior fronto-occipital fasciculus; ILF, inferior longitudinal fasciculus; l-MCI, late mild cognitive impairment; MD, mean diffusivity; MDP, maximum density path; MMSE, Mini-Mental State Examination; UNC, uncinate fasciculus. (For interpretation of the references to color in this Figure, the reader is referred to the web version of this article.)

Table 4
Average results from 10 runs of an SVM, 10 × 10-fold cross-validated classification with different sets of features. Average accuracy, sensitivity, and specificity are shown as percentages followed by the maximum from the 10 runs

Classification	Features	Percent accuracy (maximum)	Percent sensitivity (maximum)	Percent specificity (maximum)
CTL/AD	FA (n = 1080)	74.5 ± 1.3 (77.0)	75.0 ± 1.4 (78.0)	73.9 ± 2.2 (75.7)
	MD (n = 1080)	80.6 ± 2.3 (85.1)	79.2 ± 3.2 (86.0)	82.4 ± 3.4 (89.2)
	$FA_{FDR\ CvA}$ (n = 214)	77.8 ± 1.3 (79.3)	78.2 ± 2.0 (80.0)	77.3 ± 1.4 (78.4)
	$MD_{FDR\ CvA}$(n = 641)	84.9 ± 0.8 (86.2)	84.4 ± 2.1 (88.0)	85.7 ± 1.8 (89.2)
CTL/l-MCI	MD (n = 1080)	68.3 ± 2.6 (70.8)	69.8 ± 3.8 (76.0)	66.4 ± 4.1 (74.4)
	$MD_{FDR\ CvL}$ (n = 12)	79.0 ± 1.3 (82.0)	76.9 ± 1.8 (80.0)	81.5 ± 2.9 (84.6)

Key: AD, Alzheimer's disease; CTL, controls; FA, fractional anisotropy; FDR, false discovery rate; l-MCI, late mild cognitive impairment; MD, mean diffusivity; SVM, support vector machine.

3.2. SVM results

Table 4 shows the percent accuracy, sensitivity, and specificity of the 2 classifications using different subsets of features. Because of this randomized training, results could differ on each SVM run. We therefore report an average of 10 different runs. Overall, MD features performed better than FA features. Further reducing dimensionality, by only choosing the mean MDP points that passed FDR, increased the accuracy.

4. Discussion

In this article, we apply a novel tract clustering and compact fiber representation method that may be a useful tool for understanding the effects of AD on the brain's WM circuitry. It combines some of the benefits of tractography-based methods with those of voxel-based analyses, by providing spatial detail in defining statistical associations. It does not rely exclusively on global registration of the images into the same space, but it explicitly models white matter tracts based on anatomic prior information. We were able to compute tract-specific mean shapes in a space that is invariant to scaling, translation, and rotation. On the other hand, other methods for DTI analysis, such as TBSS (Smith et al., 2006), do not compute correspondences between explicit models of tracts but rely on extrema in the FA maps to identify features across subjects, which may differ in their homology. In addition to this, unlike other WM tract clustering analysis registration methods that either use Procrustes fitting (Corouge et al., 2006), which does not take shape into account, or use linear matching (Colby et al., 2012), where the points across curves may not correspond, our registration method optimally resamples each subject's tract geometry by taking into account its geodesics when registering to the corresponding computed mean tract. This reduces the bias and increases the accuracy. Each tract's mean representation offers an efficient method to reduce the white matter map's high voxelwise dimensionality to a set of points that can capture relevant macroanatomic and microstructural information.

In this method, we assess DTI metrics along tracts (Table 3; Fig. 2) taking into account within tract variability to tease apart whole tract and more focal abnormalities. In many tractography analyses, the microstructural metrics (e.g., FA, MD, and so forth) along one tract are collapsed down to a single mean scalar value for statistics, resulting in a loss of information and perhaps power to detect group differences if they are in fact more localized (of course, the tract mean may also be valuable and can be computed from our method). Using the MDP method, we detected significant WM deficits in AD patients and l-MCI subjects relative to cognitively healthy CTL subjects as might be expected from the DTI literature on AD (Braskie and Thompson, 2014; Nir et al., 2013). We found higher MD and lower FA along the MDPs of many WM tracts previously implicated in AD (Fellgiebel et al., 2008; Stebbins and Murphy, 2009), implying disrupted WM microstructure. More subtle l-MCI deficits were found in temporal (right cingulum of the hippocampus and the left uncinate fasciculus and inferior longitudinal fasciculus) and posterior (lingual gyrus and precuneus corpus callosum) tracts of the brain, corroborating a pattern of degeneration in the temporal lobe and posterior temporo-parietal circuitry found in many other DTI studies of MCI and AD (Chua et al., 2008; Head et al., 2004; Stahl et al., 2007; Stebbins and Murphy, 2009). These regions are consistent with regions showing earliest pathologic changes (Braak and Braak, 1996; Thompson et al., 2007). Only MD measures were sensitive enough to detect l-MCI differences and revealed more profuse associations than FA in all analyses (Table 3). This is in line with many prior studies. A recent AD DTI review found that MD values have more discriminative power than FA values and higher effect sizes for detecting disease related effects, derived from 55 different studies, in the frontal, parietal, occipital, and temporal lobes (Clerx et al., 2012; Nir et al., 2013). We also found significant associations between FA and MD MDP measures and cognitive deficits, as measured by MMSE scores, across all subjects. Overall, both FA and MD showed significant associations. Although MD showed widespread significance (Fig. 2), disease effects on FA were detected only in localized regions of tracts; these locale could be lost with whole tract averages.

The detection of a disease effect in one part of a tract does not mean that the disease selectively affects that part of the tract—the biology of degenerative brain diseases such as AD suggests a relentless spread in which all parts of all fibers in the brain are progressively affected. However, some neuroanatomical and technical factors may make disease effects (or any effects) harder to detect in some parts of tracts than others. For instance, some parts of the tracts have low signal to noise ratio for the measures examined here, either because of localized signal distortions during image acquisition or anatomic white matter complexity, such as fanning or fiber crossing. The power of localized analysis includes the ability to detect effects where there is greatest power to detect them but does not necessarily mean the scope of pathology has been fully mapped or that it is as anatomically selective as the maps might imply.

As with any clinical data set, we must take into account the potential for increased noise and processing difficulties in pathologic scans. In AD, reconstruction of the local intra-voxel fiber structure is more susceptible to error because of altered WM microstructure (demyelination, axonal injury, and cerebrovascular microinfarcts). This method relies on accurate tractography best achieved by using the full information of the CSA-ODFs to reconstruct the diffusion signal in regions where WM morphology is highly altered. Additionally, the quality of registration between the JHU atlas and images with atrophied tissue (e.g., larger ventricles and sulci) may not be optimal.

A range of MRI modalities have been used in conjunction with machine learning techniques to track MCI and AD progression. Volumetric approaches, including hippocampal volume, gray matter volume from voxel-based morphometry, and cortical thickness (Desikan et al., 2009; Klöppel et al., 2008; Lerch et al., 2008; Magnin et al., 2009) have effectively classified AD patients. Few studies have used DTI derived biomarkers for SVM classification purposes. In a sample of 27 subjects, tractography-based connectivity metrics based on fiber count, anisotropy, and diffusivity measures were used to classify AD with an accuracy of 88% (Wee et al., 2011). Some studies have also used features derived from full DTI maps and TBSS skeletons using methods like Pearson correlation and ReliefF (Pearson et al., 1985; Robnik-Šikonja and Kononenko, 2003) to reduce the number of features (Graña et al., 2011; Haller at al., 2010; O'Dwyer et al., 2012), yielding accuracies of more than 90%. In this study, we evaluated 200 subjects and were able to reach relatively high accuracy despite the heterogeneity of our sample (more than 14 scanners across the country) and using the full set of features from the compact mean MDP representation. The features interpolated along our full mean MDPs are robust enough to reach high classification accuracies (approximately 80%), so that reducing dimensionality by including only statistically significant MDP points did not dramatically increase classification accuracy (approximately 85%).

Ultimately, this novel method may reduce bias and increase accuracy using optimal tract geometry resampling. It allows us to project and compare any number of novel measures on the MDPs. We are additionally able to train and classify SVMs successfully based on features mapped onto these anatomically correct white

matter tract representations. In the future, mapping other microstructural biomarkers, such as fiber density and novel HARDI-ODF derived biomarkers such as GFA, QFA and tensor distribution function measures (Leow et al. 2009; Tuch et al. 2004; Yeh et al. 2010; Zhan et al. 2009) along the MDPs may further our ability to distinguish patients from controls based on diffusion-weighted imaging data. Furthermore, ADNI2 is a longitudinal study and, as it progresses, we will be able to investigate which subjects develop AD, and if these early WM aberrations help predict future deficits and conversion to AD. This study offers initial evidence that DTI-based measures along MDPs may be a novel biomarker of AD.

Disclosure statement

The authors have no potential financial or personal conflicts of interest including relationships with other people or organizations within 3 years of beginning the work submitted that could inappropriately influence this work. One of the authors, Michael Weiner, receives private funding unrelated to the content of this article.

Acknowledgements

Algorithm development and image analysis for this study was funded, in part, by grants to Paul Thompson from the National Institute of Biomedical Imaging and Bioengineering (R01 EB008281, R01 EB008432) and by the National Institute on Aging, National Institute of Biomedical Imaging and Bioengineering, National Institute of Mental Health, the U.S. National Library of Medicine, and the National Center for Research Resources (AG016570, AG040060, EB01651, MH097268, LM05639, RR019771 to Paul Thompson). Data collection and sharing for this project was funded by ADNI (National Institutes of Health grant U01 AG024904). ADNI is funded by the National Institute on Aging, the National Institute of Biomedical Imaging and Bioengineering, and through contributions from the following: Abbott; Alzheimer's Association; Alzheimer Drug Discovery Foundation; Amorfix Life Sciences Ltd; AstraZeneca; Bayer HealthCareBayer HealthCare; BioClinica, Inc; Biogen; Bristol-Myers Squibb Foundation; Eisai; Elan; Eli Lilly and Company; F. Hoffmann-La Roche Ltd, and its affiliated company Genentech Foundation; GE Healthcare; Innogenetics, N.V.; IXICO Ltd; Janssen Alzheimer Immunotherapy Research & Development, LLC; Johnson & Johnson Pharmaceutical Research & Development LLC; Medpace, Inc; Merck & Co, Inc; Meso Scale Diagnostics, LLC; Novartis; Pfizer; Servier; Synarc Inc; and Takeda Pharmaceutical North America. The Canadian Institutes of Health Research is providing funds to support ADNI clinical sites in Canada. Private sector contributions are facilitated by the Foundation for the National Institutes of Health. The grantee organization is the Northern California Institute for Research and Education, and the study is coordinated by the Alzheimer's Disease Cooperative Study at the University of California, San Diego. ADNI data are disseminated by the Laboratory for Neuro Imaging at the University of Southern California. This research was also supported by National Institutes of Health grants P30 AG010129 and K01 AG030514 from the National Institute of General Medical Sciences.

References

Aganj, I., Lenglet, C., Jahanshad, N., Yacoub, E., Thompson, P.M., Sapiro, G., 2011. A Hough transform global probabilistic approach to multiple-subject diffusion MRI tractography. Med. Image Anal. 15, 414–425.

Aganj, I., Lenglet, C., Sapiro, G., Yacoub, E., Ugurbil, K., Harel, N., 2010. Reconstruction of the orientation distribution function in single- and multiple-shell q-ball imaging within constant solid angle. Magn. Reson. Med. 64, 554–566.

Alzheimer's Association, 2011. Alzheimer's disease facts and figures. Alzheimer's Dement. 8, 1–72.

Basser, P.J., Mattiello, J., LeBihan, D., 1994. MR diffusion tensor spectroscopy and imaging. Biophys. J. 66, 259–267.

Benjamini, Y., Hochberg, Y., 1995. Controlling the false discovery rate - a practical and powerful approach to multiple testing. J. R. Stat. Soc. Ser. B (Methodological) 57, 289–300.

Braak, H., Braak, E., 1996. Development of Alzheimer-related neurofibrillary changes in the neocortex inversely recapitulates cortical myelogenesis. Acta Neuropathol. 92, 197–201.

Braskie, M.N., Thompson, P.M., 2014. A focus on structural brain imaging in the Alzheimer's Disease Neuroimaging Initiative. Biol. Psychiatry 75, 527–533.

Brun, A., Englund, E., 1986. White matter disorder in dementia of the Alzheimer type: a pathoanatomical study. Ann. Neurol. 19, 253–262.

Cetingul, H.E., Wright, M.J., Thompson, P.M., Vidal, R., 2014. Segmentation of high angular resolution diffusion MRI using sparse Riemannian manifold clustering. IEEE Trans. Med. Imaging 33, 301–317.

Chew, H., Bogner, R., Lim, C., 2001. Dual v-support vector machine with error rate and training size biasing. IEEE Int. Conf. Acoustics, Speech, Signal Process. 2, 1269–1272.

Chua, T.C., Wen, W., Slavin, M.J., Sachdev, P.S., 2008. Diffusion tensor imaging in mild cognitive impairment and Alzheimer's disease: a review. Curr. Opin. Neurol. 21, 83–92.

Clerx, L., Visser, P.J., Verhey, F., Aalten, P., 2012. New MRI markers for Alzheimer's disease: a meta-analysis of diffusion tensor imaging and a comparison with medial temporal lobe measurements. J. Alzheimer's Dis. 29, 405–429.

Colby, J., Soderberg, L., Lebel, C., Dinov, I.D., Thompson, P.M., Sowell, E.R., 2012. Along- tract statistics allow for enhanced tractography analysis. Neuroimage 59, 3227–3242.

Cortes, C., Vapnik, V., 1995. Support-vector networks. Mach. Learn. 20, 273–297.

Corouge, I., Fletcher, P.T., Joshi, S., Gouttard, S., Gerig, G., 2006. Fiber tract-oriented statistics for quantitative diffusion tensor MRI analysis. Med. Image Anal. 10, 786–798.

Daducci, A., Canales-Rodriguez, E., Descoteaux, M., Gur, Y., Mani, M., Merlet, S., Ramirez-Manzanares, A., Rodrigues, P., Reisert, M., Sepehrband, F., 2014. Quantitative comparison of reconstruction methods for intra-voxel fiber recovery from diffusion MRI. IEEE Trans. Med. Imaging 33, 384–399.

Delbeuck, X., Van der Linden, M., Collette, F., 2003. Alzheimer's disease as a disconnection syndrome? Neuropsychol. Rev. 13, 79–92.

Desikan, R.S., Cabral, H.J., Hess, C.P., Dillon, W.P., Glastonbury, C.M., Weiner, M.W., Schmansky, N.J., Greve, D.N., Salat, D.H., Buckner, R.L., Fischl, B., Alzheimer's Disease Neuroimaging Initiative, 2009. Automated MRI measures identify individuals with mild cognitive impairment and Alzheimer's disease. Brain 132, 2048–2057.

Dijkstra, E.W., 1959. A note on two problems in connexion with graphs. Numerische Mathematik 1, 269–271.

Fellgiebel, A., Schermuly, I., Gerhard, A., Keller, I., Albrecht, J., Weibrich, C., Müller, M.J., Stoeter, P., 2008. Functional relevant loss of long association fibre tracts integrity in early Alzheimer's disease. Neuropsychologia 46, 1698–1706.

Fillard, P., Arsigny, W., Pennec, X., Hayashi, K.M., Thompson, P.M., Ayache, N., 2006. Measuring brain variability by extrapolating sparse tensor fields measured on sulcal lines. Neuroimage 34, 639–650.

Fischl, B., van der Kouwe, A., Destrieux, C., Halgren, E., Segonne, F., Salat, D.H., Busa, E., Seidman, L.J., Goldstein, J., Kennedy, D., Caviness, V., Makris, N., Rosen, B., Dale, A.M., 2004. Automatically parcellating the human cerebral cortex. Cereb. Cortex 14, 11–22.

Folstein, M.F., Folstein, S.E., McHugh, P.R., 1975. "Mini-mental state". A practical method for grading the cognitive state of patients for the clinician. J. Psychiatr. Res. 12, 189–198.

Graña, M., Termenon, M., Savio, A., Gonzalez-Pinto, A., Echeveste, J., Pérez, J.M., Besga, A., 2011. Computer aided diagnosis system for Alzheimer disease using brain diffusion tensor imaging features selected by Pearson's correlation. Neurosci. Lett. 502, 225–229.

Haller, S., Nguyen, D., Rodriguez, C., Emch, J., Gold, G., Bartsch, A., Lovblad, K.O., Giannakopoulos, P., 2010. Individual prediction of cognitive decline in mild cognitive impairment using support vector machine-based analysis of diffusion tensor imaging data. J. Alzheimers Dis. 22, 315–327.

Head, D., Buckner, R.L., Shimony, J.S., Williams, L.E., Akbudak, E., Conturo, T.E., McAvoy, M., Morris, J.C., Snyder, A.Z., 2004. Differential vulnerability of anterior white matter in nondemented aging with minimal acceleration in dementia of the Alzheimer type: evidence from diffusion tensor imaging. Cereb. Cortex 14, 410–423.

Holmes, C.J., Hoge, R., Collins, L., Woods, R., Toga, A.W., Eva, A.C., 1998. Enhancement of MR images using registration for signal averaging. J. Comput. Assist. Tomogr. 22, 324–333.

Hua, X., Lee, S., Hibar, D.P., Yanovsky, I., Leow, A.D., Toga, A.W., Jack Jr., C.R., Bernstein, M.A., Reiman, E.M., Harvey, D.J., Kornak, J., Schuff, N., Alexander, G.E., Weiner, M.W., Thompson, P.M., 2010. Mapping Alzheimer's disease progression in 1309 MRI scans: power estimates for different inter-scan intervals. Neuroimage 51, 63–75.

Hua, X., Leow, A.D., Lee, S., Klunder, A.D., Toga, A.W., Lepore, N., Chou, Y.Y., Brun, C., Chiang, M.C., Barysheva, M., Jack Jr., C.R., Bernstein, M.A., Britson, P.J., Ward, C.P., Whitwell, J.L., Borowski, B., Fleisher, A.S., Fox, N.C., Boyes, R.G., Barnes, J., Harvey, D., Kornak, J., Schuff, N., Boreta, L., Alexander, G.E., Weiner, M.W., Thompson, P.M., Alzheimer's Disease Neuroimaging Initiative,

2008. 3D characterization of brain atrophy in Alzheimer's disease and mild cognitive impairment using tensor-based morphometry. Neuroimage 41, 19–34.
Hua, K.J., Zhang, J., Wakana, S., Jiang, H., Li, X., Reich, D.S., Calabresi, P.A., Pekar, J.J., van Zijl, P.C., Mori, S., 2008. Tract probability maps in stereotaxic spaces: analyses of white matter anatomy and tract-specific quantification. Neuroimage 39, 336–347.
Iglesias, J.E., Liu, C.Y., Thompson, P.M., Tu, Z., 2011. Robust brain extraction across datasets and comparison with publicly available methods. IEEE Trans. Med. Imaging 30, 1617–1634.
Jahanshad, N., Prasad, G., Toga, A.W., McMahon, K.L., de Zubicaray, G.I., Martin, N.G., Wright, M.J., Thompson, P.M., 2012. Genetics of path lengths in brain connectivity networks: HARDI-based maps in 457 adults. MICCAI MBIA 2012, 29–40.
Jahanshad, N., Zhan, L., Bernstein, M.A., Borowski, B., Jack, C.R., Toga, A.W., Thompson, P.M., 2010. Diffusion tensor imaging in seven minutes: determining trade-offs between spatial and directional resolution. Proc. IEEE Int. Symp. Biomed. Imaging 2010, 1161–1164.
Jenkinson, M., Bannister, P., Brady, J., Smith, S., 2002. Improved optimisation for the robust and accurate linear registration and motion correction of brain images. Neuroimage 17, 825–841.
Joshi, S.H., Klassen, E., Srivastava, A., Jermyn, I., 2007a. Removing shape-preserving transformations in square-root elastic (SRE) framework for shape analysis of curves. Proc. IEEE Comput. Soc. Conf. Compu. Vis. Pattern Recognit. 4679, 387–398.
Joshi, S.H., Klassen, E., Srivastava, A., Jermyn, I., 2007b. A novel representation for Riemannian analysis of elastic curves in Rn. Proc. IEEE Comput. Soc. Conf. Compu. Vis. Pattern Recognit. 2007, 1–7.
Kim, Y., Thompson, P.M., Toga, A.W., Vese, L., Zhan, L., 2009. HARDI denoising: variational regularization of spherical apparent diffusion coefficient sADC. Inf. Process. Med. Imaging 21, 515–527.
Klöppel, S., Stonnington, C.M., Chu, C., Draganski, B., Scahill, R.I., Fox, N.C., Jack, C.R., Ashburner, J., Frackowiak, R.S.J., 2008. Automatic classification of MR scans in Alzheimer's disease. Brain 131, 681–689.
Leow, A.D., Yanovsk, I., Chiang, M.C., Lee, A.D., Klunder, A., Lu, A., Becker, J., Davis, S., Toga, A.W., Thompson, P.M., 2007. Statistical properties of Jacobian maps and the realization of unbiased large-deformation nonlinear image registration. IEEE Trans. Med. Imaging 26, 822–832.
Leow, A.D., Zhu, S., Zhan, L., McMahon, K., de Zubicaray, G.I., Meredith, M., Wright, M.J., Toga, A.W., Thompson, P.M., 2009. The tensor distribution function. Magn. Reson. Med. 61, 205–214.
Lerch, J.P., Pruessner, J., Zijdenbos, A.P., Collins, D.L., Teipel, S.J., Hampel, H., Evans, A.C., 2008. Automated cortical thickness measurements from MRI can accurately separate Alzheimer's patients from normal elderly controls. Neurobiol. Aging 29, 23–30.
Liu, Y., Spulber, G., Lehtimäki, K.K., Könönen, M., Hallikainen, I., Gröhn, H., Kivipelto, M., Hallikainen, M., Vanninen, R., Soininen, H., 2011. Diffusion tensor imaging and tract-based spatial statistics in Alzheimer's disease and mild cognitive impairment. Neurobiol. Aging 32, 1558–1571.
Maddah, M., Zollei, L., Grimson, W.E.L., Wells, W.M., 2008. Modeling of anatomical information in clustering of white matter fiber trajectories using Dirichlet distribution. Proc. Workshop Math. Methods Biomed. Image Analysis 2008, 1–7.
Magnin, B., Mesrob, L., Kinkingnéhun, S., Pélégrini-Issac, M., Colliot, O., Sarazin, M., Dubois, B., Lehéricy, S., Benali, H., 2009. Support vector machine-based classification of Alzheimer's disease from whole-brain anatomical MRI. Neuroradiology 51, 73–83.
Medina, D., DeToledo-Morrell, L., Urresta, F., Gabrieli, J.D., Moseley, M., Fleischman, D., Bennett, D.A., Leurgans, S., Turner, D.A., Stebbins, G.T., 2006. White matter changes in mild cognitive impairment and AD: a diffusion tensor imaging study. Neurobiol. Aging 27, 663–672.
Migliaccio, R., Agosta, F., Possin, K.L., Rabinovici, G.D., Miller, B.L., Gorno-Tempini, M.L., 2012. White matter atrophy in Alzheimer's disease variants. Alzheimers Dement. 8 (5 Suppl), S78–S87 e1–2.
Nir, T.M., Jahanshad, N., Villalon-Reina, J.E., Toga, A.W., Jack, C.R., Weiner, M.W., Thompson, P.M., Alzheimer's Disease Neuroimaging Initiative (ADNI), 2013. Effectiveness of regional DTI measures in distinguishing Alzheimer's disease, MCI, and normal aging. Neuroimage Clin. 3, 180–195.
O'Donnell, L., Kubicki, M., Shenton, M.E., Dreusicke, M.H., Grimson, W.E., Westin, C.F., 2006. A method for clustering white matter fiber tracts. AJNR Am. J. Neuroradiol. 27, 1032–1036.
O'Dwyer, L., Lamberton, F., Bokde, A.L.W., Ewers, M., Faluyi, Y.O., Tanner, C., Mazoyer, B., O'Neill, D., Bartley, M., Collins, D.R., Coughlan, T., Prvulovic, D., Hampel, H., 2012. Using support vector machines with multiple indices of diffusion for automated classification of mild cognitive impairment. PLoS One 7, e32441.
Pearson, R.C.A., Esiri, M.M., Hiorns, R.W., Wilcock, G.K., Powell, T.P., 1985. Anatomical correlates of the distribution of the pathological changes in the neocortex in Alzheimer's disease. Proc. Natl. Acad. Sci. U.S.A 82, 4531–4534.
Prasad, G., Jahanshad, N., Aganj, I., Lenglet, C., Sapiro, G., Toga, A.W., Thompson, P.M., 2011a. Atlas-based fiber clustering for multi-subject analysis of high angular resolution diffusion imaging tractography. IEEE Int. Symp. Biomed. Imaging 2011, 276–280.
Prasad, G., Joshi, S.H., Jahanshad, N., Villalon, J., Aganj, I., Lenglet, C., Sapiro, G., McMahon, K.L., de Zubicaray, G.I., Martin, N.G., Wright, M.J., Toga, A.W., Thompson, P.M., 2011b. White matter tract analysis in 454 adults using maximum density paths. MICCAI Workshop on Computational Diffusion MRI, Toronto, Canada, 2011.
Prasad, G., Joshi, S.H., Jahanshad, N., Villalon, J., Aganj, I., Lenglet, C., Sapiro, G., McMahon, K.L., de Zubicaray, G.I., Martin, N.G., Wright, M.J., Toga, A.W., Thompson, P.M., 2014. Shape analysis of white matter tracts via maximum density paths. Neuroimage 97, 284–295.
Prasad, G., Nir, T.M., Toga, A.W., Thompson, P.M., ADNI, 2013b. Tractography density and network measures in Alzheimer's disease. Int. Symp. Biomed. Imaging. Accepted.
Robnik-Šikonja, M., Kononenko, I., 2003. Theoretical and empirical analysis of ReliefF and RReliefF. Mach. Learn 5, 23–69.
Rose, S.E., Chen, F., Chalk, J.B., Zelaya, F.O., Strugnell, W.E., Benson, M., Semple, J., Doddrell, D.M., 2000. Loss of connectivity in Alzheimer's disease: an evaluation of white matter tract integrity with colour coded MR diffusion tensor imaging. J. Neurol. Neurosurg. Psychiatry 69, 528–530.
Schwarz, C.G., Reid, R.I., Gunter, J.L., Senjem, M.L., Przybelski, S.A., Zuk, S.M., Whitwell, J.L., Vemuri, P., Josephs, K.A., Kantarci, K., Thompson, P.M., Weiner, M.W., Petersen, R.C., Jack Jr., C.R., ADNI, 2014. Improved DTI registration allows voxel-based analysis that outperforms tract-based spatial statistics. Neuroimage 94, 65–78.
Shi, Y., Tu, Z., Reiss, A.L., Dutton, R.A., Lee, A.D., Galaburda, A.M., Dinov, I.D., Thompson, P.M., Toga, A.W., 2007. Joint sulci detection on cortical surfaces with graphical models and boosted priors. IEEE Trans. Med. Imaging 28, 361–373.
Sjobeck, M., Haglund, M., Englund, E., 2005. Decreasing myelin density reflected increasing white matter pathology in Alzheimer's disease-a neuropathological study. Int. J. Geriatr. Psychiatry 20, 919–926.
Smith, S.M., 2002. Fast robust automated brain extraction. Hum. Brain Mapp. 17, 143–155.
Smith, S.M., Jenkinson, M., Johansen-Berg, H., Rueckert, D., Nichols, T.E., Mackay, C.E., Watkins, K.E., Ciccarelli, O., Cader, M.Z., Matthews, P.M., Behrens, T.E., 2006. Tract-based spatial statistics: voxelwise analysis of multi-subject diffusion data. Neuroimage 31, 1487–1505.
Stahl, R., Dietrich, O., Teipel, S.J., Hampel, H., Reiser, M.F., Schoenberg, S.O., 2007. White matter damage in Alzheimer disease and mild cognitive impairment: assessment with diffusion-tensor MR imaging and parallel imaging techniques. Radiology 243, 483–492.
Stebbins, G.T., Murphy, C.M., 2009. Diffusion tensor imaging in Alzheimer's disease and mild cognitive impairment. Behav. Neurol. 21, 39–49.
Thompson, P.M., Hayashi, K.M., Dutton, R.A., Chiang, M.C., Leow, A.D., Sowell, E.R., de Zubicaray, G., Becker, J.T., Lopez, O.L., Aizenstein, H.J., Toga, A.W., 2007. Tracking Alzheimer's disease. Ann. N. Y. Acad. Sci. 1097, 183–214.
Thompson, P.M., Schwartz, C., Lin, R.T., Khan, A.A., Toga, A.W., 1996a. 3D statistical analysis of sulcal variability in the human brain. J. Neurosci 16, 4261–4274.
Thompson, P.M., Schwartz, C., Toga, A.W., 1996b. High-resolution random mesh algorithms for creating a probabilistic 3D surface atlas of the human brain. Neuroimage 3, 19–34.
Tong, M., Kim, Y., Zhan, L., Sapiro, G., Lenglet, C., Mueller, B., Thompson, P.M., Vese, L., 2012. A variational model for denoising high angular resolution diffusion imaging data. Proc. IEEE Int. Symp. Biomed. Imaging 2012, 530–533.
Tuch, D.S., 2004. Q-ball imaging. Magn. Reson. Med. 52, 1358–1372.
Tustison, N., Avants, B., Cook, P., Kim, J., Whyte, J., Gee, J., Stone, J., 2014. Logical circularity in voxel-based analysis: normalization strategy may induce statistical bias. Hum. Brain Mapp. 35, 745–759.
Wassermann, D., Kanterakis, E., Gur, R.C., Deriche, R., Verma, R., 2010. Diffusion-based population statistics using tract probability maps. Med. Image Comput. Comput. Assist. Interv. 13, 631–639.
Wee, C.Y., Yap, P.T., Li, W., Denny, K., Browndyke, J.N., Potter, G.G., Welsh-Bohmer, K.A., Wang, L., Shen, D., 2011. Enriched white matter connectivity networks for accurate identification of MCI patients. Neuroimage 54, 1812–1822.
Yeh, F.C., Wedeen, V.J., Tseng, W.Y., 2010. Generalized q-sampling imaging. IEEE Trans. Med. Imaging 29, 1626–1635.
Zhan, L., Jahanshad, N., Ennis, D.B., Jin, Y., Bernstein, M.A., Borowski, B.J., Jack Jr., C.R., Toga, A.W., Leow, A.D., Thompson, P.M., 2013. Angular versus spatial resolution trade-offs for diffusion imaging under time constraints. Hum. Brain Mapp. 34, 2688–2706.
Zhan, L., Leow, A.D., Zhu, S., Barysheva, M., Toga, A.W., McMahon, K.L., de Zubicaray, G.I., Wright, M.J., Thompson, P.M., 2009. A novel measure of fractional anisotropy based on the tensor distribution function. Med. Image. Comput. Comput. Assist. Interv. 12 (Pt 1), 845–852.
Zhou, Y., Thompson, P.M., Toga, A.W., 1999. Automatic extraction and parametric representations of cortical sulci. Comput. Graph. Appl 19, 49–55.